NANO LETTERS

Letter

pubs.acs.org/NanoLett

Nucleation Control for Large, Single Crystalline Domains of Monolayer Hexagonal Boron Nitride via Si-Doped Fe Catalysts

Sabina Caneva,[†] Robert S. Weatherup,[†] Bernhard C. Bayer,[†,‡] Barry Brennan,[§] Steve J. Spencer,[§] Ken Mingard,[§] Andrea Cabrero-Vilatela,[†] Carsten Baehtz,[∥] Andrew J. Pollard,[§] and Stephan Hofmann*[,†]

[†]Department of Engineering, University of Cambridge, JJ Thomson Avenue, CB3 0FA, Cambridge, United Kingdom

[‡]Faculty of Physics, University of Vienna, Boltzmanngasse 5, A-1090 Vienna, Austria

[§]National Physical Laboratory, Hampton Rd, TW11 0LW, Teddington, Middlesex, United Kingdom

[∥]Institute of Ion Beam Physics and Materials Research, Helmholtz-Zentrum Dresden-Rossendorf, 01314 Dresden, Germany

Supporting Information

ABSTRACT: The scalable chemical vapor deposition of monolayer hexagonal boron nitride (h-BN) single crystals, with lateral dimensions of ~0.3 mm, and of continuous h-BN monolayer films with large domain sizes (>25 μm) is demonstrated via an admixture of Si to Fe catalyst films. A simple thin-film Fe/SiO_2/Si catalyst system is used to show that controlled Si diffusion into the Fe catalyst allows exclusive nucleation of monolayer h-BN with very low nucleation densities upon exposure to undiluted borazine. Our systematic in situ and ex situ characterization of this catalyst system establishes a basis for further rational catalyst design for compound 2D materials.

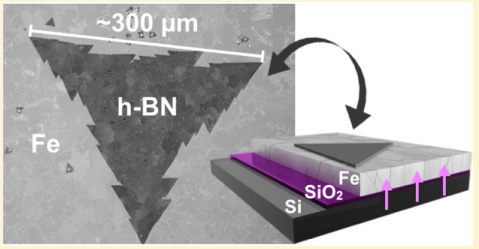

KEYWORDS: *Hexagonal boron nitride (h-BN), chemical vapor deposition (CVD), borazine $(HBNH)_3$, in situ X-ray diffraction (XRD), secondary ion mass spectrometry (SIMS), Fe catalyst*

The technological potential of atomically thin, two-dimensional (2D) materials, including graphene, hexagonal boron nitride (h-BN), transition metal dichalcogenides, and the numerous possible 2D heterostructures, is currently limited by the lack of scalable growth control. Critical parameters to be controlled for "electronic-grade" 2D materials include the number of layers, stoichiometry, and crystal structure, i.e., domain size, connectivity, and orientation.[1−3] Significant progress in the large area, high-quality manufacture of graphene in particular has been made by catalytic chemical vapor deposition (CVD).[1,4] Essential to growth control for 2D material CVD is an understanding of the underlying growth mechanisms, specifically the interactions of the precursors and growing 2D structure with the catalyst.[5−7] The 2D domain size and distribution are thereby linked to nucleation control.[8−10] Catalyst engineering, in particular designing surface and bulk alloy catalysts, has been demonstrated to allow such nucleation control for graphene CVD.[8,10,11] Most other application-relevant 2D materials such as h-BN are compounds, which means that their controlled CVD is inherently more complex as two elements need to be fed.[12] The lack of understanding of such multicomponent materials systems is reflected in the so far limited control over scalable growth.

h-BN, isostructural to graphene but with alternating B and N atoms arranged in its monolayer honeycomb structure, is technologically promising as an ultrathin dielectric-, support-, or barrier-layer in particular for integrated electronics and photonics.[13] CVD of h-BN is seen as the most promising deposition method and has been reported on a range of transition catalyst metals, including Cu,[12,14−17] Pt,[18−20] Ni,[21−23] and Co[24] polycrystalline films and foils, as well as on Fe,[25] Pd,[26] Pt,[27] Ag,[28] Ir,[29] Mo,[30] Ru,[31] and Rh[32] single crystals, with early reports of multilayer h-BN CVD dating back to the 1970s.[33] Among the largest as-grown h-BN single crystals to date are hexagonal domains with areas of the order of ~35 μm^2 reported for electropolished Cu foils,[34] but due to the limited understanding of the growth process there is currently no consensus as to which catalyst offers most growth control and the highest h-BN quality. It is important to note that the constituent element incorporation mechanisms, i.e., for B and N, are catalyst-mediated and can be element-specific even for stoichiometric precursors such as borazine.[35−37] For instance, Cu dissolves B but not N during h-BN CVD.[12] Due to this growth complexity and the vast parameter space of CVD, catalyst engineering and optimization remain extremely challenging for compound 2D nanomaterials such as h-BN.

Here we establish a simple thin-film catalyst system, based on physical vapor deposited Fe on an oxidized Si wafer support, which allows us to significantly improve nucleation and growth control for h-BN CVD. By combining in situ X-ray diffraction (XRD) with ex-situ secondary ion mass spectrometry (SIMS) and X-ray photoelectron spectroscopy (XPS), we show that depending on the SiO_2 thickness a controlled amount of Si diffuses into the Fe catalyst upon annealing. This Si admixture,

Received: December 4, 2014
Revised: January 30, 2015
Published: February 9, 2015

DOI: 10.1021/nl5046632
Nano Lett. 2015, 15, 1867−1875

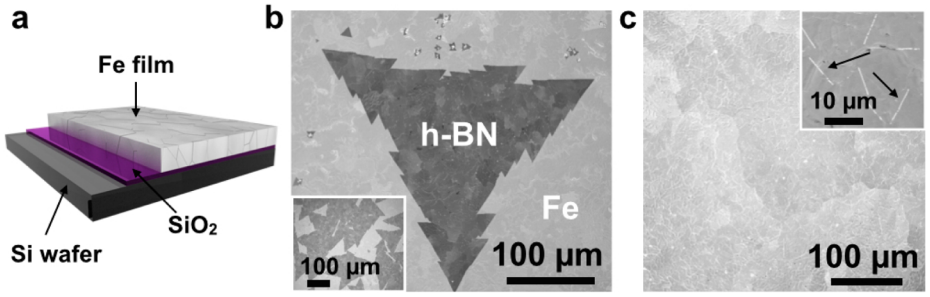

Figure 1. (a) Schematic of catalyst system composed of Fe/SiO_2/Si. (b) SEM image of a large, tooth-edged h-BN domain grown at 940 °C and 1 × 10^{-3} mbar borazine exposure for 5 min (standard conditions) on Fe(1000 nm)/SiO_2(300 nm)/Si substrates. Inset: corresponding low magnification SEM image. (c) Continuous h-BN film homogeneously covering the Fe surface after 5 min of higher pressure borazine exposure (6 × 10^{-3} mbar) at 940 °C. The individual domain boundaries can be easily identified, as indicated by the black arrows (top right inset).

albeit just at trace levels, allows us to exclusively nucleate monolayer h-BN with very low nucleation densities upon exposure of the Fe surface to undiluted borazine. For optimized CVD conditions we demonstrate h-BN single crystal domains with lateral dimensions of ~0.3 mm as well as continuous h-BN monolayer films with large domain sizes (>25 μm), as characterized by a combination of Raman spectroscopy, transmission electron microscopy (TEM), selected area electron diffraction (SAED), and atomic force microscopy (AFM). We believe that the understanding developed for this catalyst system establishes a basis for further rational catalyst design for controlled compound 2D material CVD.

Results. We adopt a simple CVD process based on an initial H_2 annealing step, a subsequent isothermal exposure in undiluted borazine and cooling in vacuum (see Methods). Figure 1a schematically shows our thin film catalyst system. The central idea thereby is that depending on the thickness of the SiO_2 a controlled amount of Si will diffuse into the Fe catalyst upon annealing. We systematically varied the SiO_2 thickness between ~1 nm (native oxide) and 2000 nm, with a Fe catalyst thickness of 1000 nm (unless otherwise stated). We adopt the following substrate nomenclature: Fe(thickness)/SiO_2(thickness)/Si substrate, with the Fe being on top of the thin-film stack (Figure 1a). Figure 1b,c shows that under optimized CVD exposure conditions very large, single-crystal monolayer h-BN domains can be achieved as well as a continuous, homogeneous monolayer h-BN film of high quality. Using a wide range of characterization techniques, we initially highlight the h-BN material quality achieved before examining in detail the growth mechanisms for this catalyst system.

Figure 1b shows postgrowth SEM analysis of the surface of a Fe(1000 nm)/SiO_2(300 nm)/Si substrate after CVD at ~940 °C and 1 × 10^{-3} mbar borazine exposure for 5 min. We observe triangular regions of constant contrast, with side lengths of ~0.3 mm, which subsequent characterization demonstrates are large, single-crystal hBN domains (Figure 2). The edges are sawtoothed with each tooth having edge length of ~30 μm. The postgrowth Fe surface was characterized using SEM channeling contrast and subsequently by crystal orientation mapping in electron backscatter diffraction (EBSD). The EBSD map in Figure S1 reveals that the structure of the Fe layer consists of body-centered-cubic Fe (α-Fe) grains with a mean size of approximately 50 μm (circle equivalent diameter) and a maximum size of about 150 μm. We note that the triangular h-BN regions, which are larger than the average Fe grains (Figure 1b inset), are continuous across numerous Fe grain boundaries. In such a case no clear overall preferred h-BN domain orientations are apparent across the numerous Fe grains, albeit h-BN domains can show alignment along specific orientations with respect to the surface of a single catalyst grain. Continuous, full h-BN monolayer coverage of the Fe surface can be achieved by using a slightly higher borazine exposure pressure (6 × 10^{-3} mbar), as shown in Figure 1c. Increasing the borazine pressure increases the h-BN nucleation density for constant temperature and growth time (Figure S2), leading to smaller triangular domain sizes for the continuous film. Nonetheless, our analysis indicates that the individual h-BN domains are >25 μm in average lateral size (inset in Figure S2c). We note that the domains grown for the higher borazine pressures no longer display sawtooth edges; however, they still preserve strict triangular shapes with straight edges.

Figure 2a,b shows TEM analysis of as-grown h-BN layers transferred to a holey carbon/copper mesh TEM grid, which verifies our above extrapolation of h-BN domain sizes by uniformity in SEM contrast. Figure 2a shows a low-resolution TEM image of a suspended h-BN film with its corresponding 6-spot diffraction pattern, indicating that the structure is crystalline with hexagonal symmetry. Additionally, the edge analysis confirms the single-layer nature of the film. Figure 2b shows selected area diffraction mapping on a large triangular h-BN domain (corresponding to Figure 1b). The diffraction patterns obtained from well-spaced areas all have identical orientation confirming the triangular regions of constant contrast are indeed single crystalline h-BN domains. Figure 2c shows an optical microscopy image of a h-BN film transferred to a SiO_2(300 nm)/Si wafer. The uniform contrast indicates the macroscopic uniformity, notwithstanding the PMMA residuals typically seen for such transfers without a subsequent cleaning step. The inset shows a transferred h-BN domain from the sample in Figure 1b and its corresponding Raman spectra (Figure 2d), exhibiting the characteristic peak at 1369 cm^{-1}, which is related to the in-plane ring vibration of h-BN.[38] Figure 2e shows the AFM analysis of the transferred h-BN domains (inset Figure 2c). The AFM image again confirms uniformity of the h-BN domain. From the step height profile at the domain edge, we extrapolate a thickness of <0.4 nm, consistent with literature values for monolayer h-BN.[17]

Key to the controlled growth of high-quality h-BN demonstrated here is the addition of trace amounts of Si to the active Fe catalyst. Figure 3 shows how the amount of Si dissolved into the Fe film can be adjusted by varying the SiO_2 interlayer thickness. Figure 3a–k compares h-BN growth for short (1 min) and longer (5 min) borazine exposures for the

DOI: 10.1021/nl5046632
Nano Lett. 2015, 15, 1867–1875

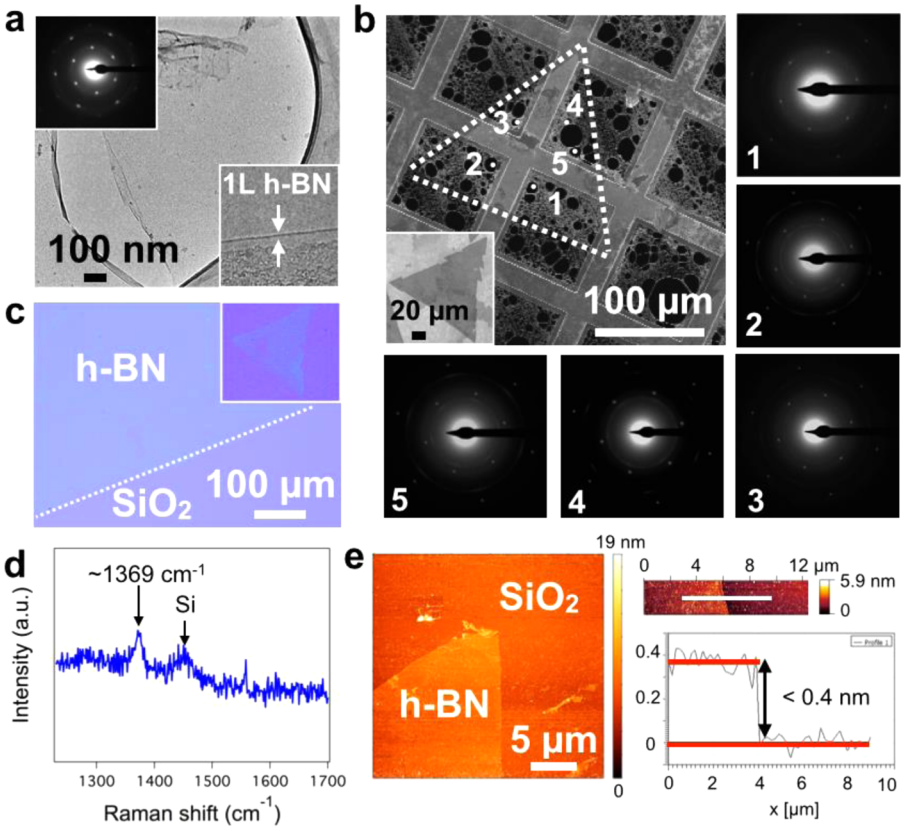

Figure 2. (a) Low-resolution TEM image of a suspended h-BN film (CVD conditions and substrate as in Figure 1b) supported on holey carbon, copper mesh TEM grid, with corresponding hexagonal electron diffraction pattern (top left inset) and edge analysis, confirming the single layer nature of the film (bottom right inset). (b) SAED study on a large triangular h-BN domain (standard CVD conditions). The SEM image shows the location of the domain (enclosed by the white dotted lines). The inset shows a similar triangle as-grown on the catalyst before transfer. The five diffraction patterns obtained from well-spaced regions of the domain have identical orientation, thus confirming it is a single crystal. (c) Optical image of a continuous h-BN film transferred onto a SiO_2(300 nm)/Si wafer via the electrochemical bubbling method. The inset shows a transferred triangular domain from the sample in Figure 1b. (d) Raman spectrum measured at the center of one of the triangular domains in c, showing the characteristic h-BN signal at 1369 cm^{-1}. The additional peak at ~1450 cm^{-1} can be attributed to third-order scattering from Si.[59] (e) AFM topography image of the tip of a h-BN triangle with detail of a domain edge (right) and corresponding step-height measurement taken at the position of the white line.

Fe(1000 nm) catalyst supported on native (~1 nm), 200, 500, and 2000 nm thick SiO_2. For the native oxide support, the postgrowth Fe surface appears extremely rough and cracked with no visible h-BN domains (Figure 3a,b). For the 200 nm thick SiO_2 support, we observe triangular h-BN domains with dimensions of the order of 20 μm after a 1 min exposure (Figure 3d). After 5 min of borazine exposure, the h-BN film almost fully covers the Fe surface. However, the sample is very inhomogeneous due to the appearance of "crater"-like features (Figure 3e). We note that these craters interrupt the continuity of the growing h-BN. This becomes more evident after transferring the sample onto a SiO_2(300)/Si wafer (Figure S3a), where holes in the h-BN film are found in the locations corresponding to the craters. For the 500 nm thick SiO_2 support, the h-BN domains are larger (80−100 μm) for 1 min exposure times (Figure 3g), and the nucleation density shows a 5-fold decrease compared to the SiO_2(200 nm) sample (Figure 3d). For longer borazine exposures the sample exhibits homogeneous h-BN coverage without "craters" emerging (Figure 3h). For the significantly thicker SiO_2 (2000 nm) support, h-BN domains with dimensions <20 μm on average are seen after 1 min (Figure 3j), and the h-BN nucleation density increases by a factor of 3 with respect to the SiO_2(500 nm) sample (Figure 3g). After 5 min borazine exposure, the Fe surface is almost completely covered (Figure 3k); however, we also observe a high density of small bright contrast regions by SEM, which correspond to h-BN multilayers (as confirmed by post-transfer optical imaging). A similar h-BN morphology is observed on sapphire- and quartz-supported Fe catalyst films (Figure S4), which exhibit a mixture of monolayer and multilayered domains.

In order to identify the origin of the variations across the samples with differing SiO_2 thicknesses, we perform postgrowth SIMS depth profiling. We note that the samples have been stored in air for two months prior to SIMS analysis. Figure 3c,f,i,l shows the distribution of Si (green dots) within the top 120 nm of the Fe catalyst surface for each of the respective SiO_2 thicknesses. For all samples the Si appears distributed within the catalyst, and within the given 1 μm spatial resolution of the technique there is no clear evidence of segregation (aside from the crater-like regions). We also note that the Si is detectable at the Fe surface for all samples. It is important to emphasize that, while SIMS allows here a detailed relative comparison of elemental distributions, absolute concentrations (e.g., of Si) could not be readily extracted from SIMS given the polycrystalline nature of the reference sample, in which different grain orientations have different sputter yields, and the unknown distributions of various oxide species throughout

DOI: 10.1021/nl5046632
Nano Lett. 2015, 15, 1867−1875

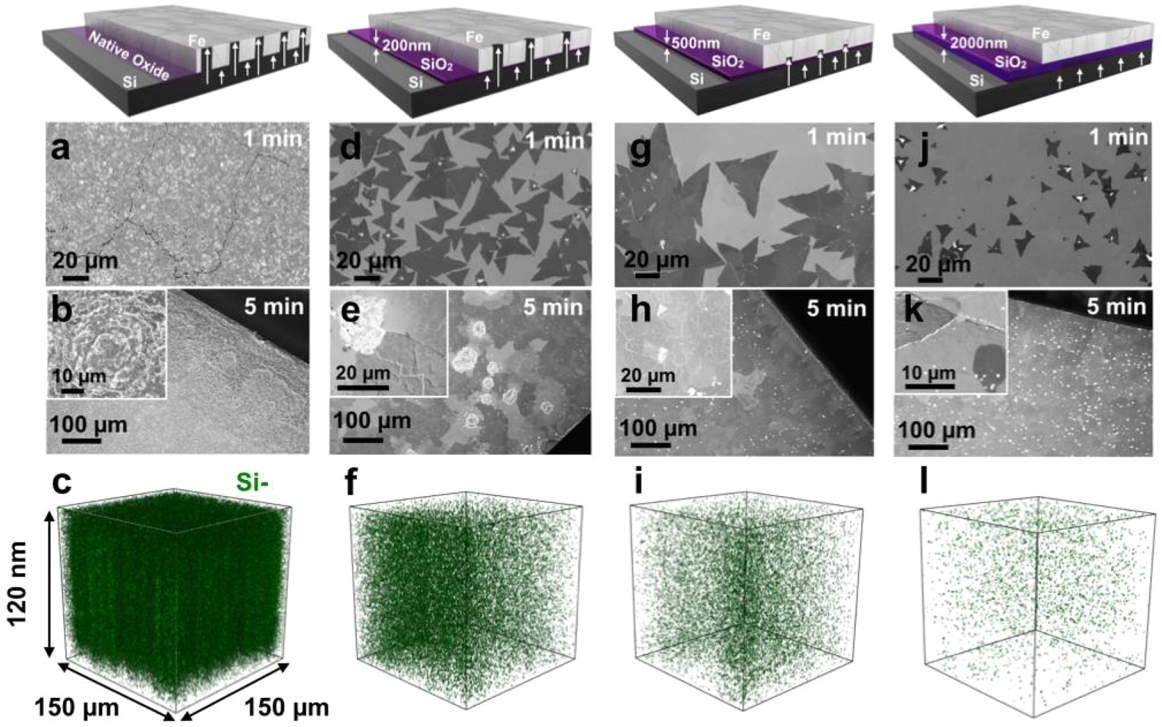

Figure 3. Schematics of the catalyst system and SEM images of the surface after growth at 940 °C and 3×10^{-3} mbar borazine exposure for 1 min (a,d,g,j) and 5 min (b,e,h,k) for Fe/SiO_2(x)/Si substrates, where x = native, 200, 500, and 2000 nm, respectively. SIMS 3D maps (c,f,i,l) showing the Si distributions in top 120 nm of the surface, corresponding to the samples respectively shown in (a,d,g,j).

the sample. The postgrowth Si^-:Fe_2^- ratio plotted as a function of depth from the Fe surface is shown in Figure S5. The SIMS analysis clearly shows that the Si^- signal decreases for increasing SiO_2 barrier thickness indicating decreasing amounts of dissolved Si. As expected, the Si content of the SiO_2(2000 nm) sample shows the lowest concentration of the processed samples with a barrier layer present, which is similar to the concentration detected for a control Fe(1000 nm)/SiO_2(500 nm)/Si substrate analyzed *before* processing (Figure S5). In order to gauge the absolute level of the Si concentrations, we perform ex situ XPS comparing the concentration of Si in the postgrowth Fe(1000 nm)/SiO_2(native)/Si and Fe(1000 nm)/SiO_2(200 nm)/Si samples. While a Si concentration of ∼20.1 at. % was estimated for the native oxide sample, the Si signal was below XPS detection limits for the 200 nm oxide sample, indicating a surface concentration of <0.1 at. %.

Important to understanding the catalytic h-BN growth mechanisms is characterization of the catalyst film evolution *during* CVD and of the interactions of B, N, and the grown h-BN with the catalyst. Figure 4a shows in situ XRD patterns that characterize the crystalline structure of the Fe catalyst during the salient stages of the CVD process. Upon annealing (∼940 °C), the body-centered-cubic (bcc, α-Fe) as-deposited Fe(500 nm) film undergoes a phase transformation to face-centered-cubic (fcc) γ-Fe (consistent with Fe phase diagram data[39,40]) and grain growth occurs (evidenced by increasing intensity and decreasing width of the reflections). Concurrently we observe the appearance of XRD signatures that can be ascribed to silicate formation (Fe_2SiO_4, Fayalite). Importantly, this silicate formation occurs upon high temperature pretreatment *prior* to the borazine exposure, and as highlighted by a comparison of surface- and bulk- sensitive scans (Figure S6), the silicates are buried in the catalyst bulk, likely at the Fe-SiO_2 interface, and not present on the surface. The appearance of a small peak at ∼18° with increasing borazine exposure time is attributed to the isothermal growth of h-BN. The catalyst phase remains predominantly γ-Fe during short (∼5 min) borazine exposures, after which the catalyst fully reverts to α-Fe upon cooling (not shown, consistent with EBSD in Figure S1). For longer borazine exposure times (∼15 min) the additional formation of a small fraction of Fe-borides (FeB and Fe_2B, located near the top surface of the catalyst films, see Figure S7) indicates that B dissolves into the Fe during CVD (although even in the case of Fe-boride formation the majority catalyst phase remains as metallic Fe, see Figure S7). The formation of structural Fe-nitrides was not observed for borazine exposure, but control experiments, in which the Fe films are exposed to undiluted NH_3 instead of borazine, suggest that nitrogen is dissolved into the surface region of the γ-Fe catalyst at the growth conditions (as indicated by Fe lattice expansion upon NH_3 addition, Figure S8). Thus, the observed isothermal h-BN growth mechanism appears linked to both B and N uptake into the Fe catalyst surface region during CVD. For longer borazine exposure times, in addition to Fe-boride formation, an isothermal transformation of the majority phase from γ-Fe to α-Fe occurs at growth temperature, which is attributed to continued B and/or Si diffusion into the Fe (Figure S9).[41] Independent of the borazine exposure time, upon cooling the majority catalyst phase reverts to α-Fe following a temperature induced phase transition (with only minor Fe-boride contributions remaining for the extended growth times).

In situ XRD indicates B and N dissolution into the Fe catalyst during h-BN growth, which we can further corroborate using postgrowth ex situ SIMS. We note that all SIMS profiles were obtained on samples that underwent only short borazine exposures (∼5 min), i.e., before in situ XRD indicates significant Fe-boride formation and isothermal γ-Fe to α-Fe transitions. Figure 4b shows the SIMS profile distribution for

DOI: 10.1021/nl5046632
Nano Lett. 2015, 15, 1867−1875

the Fe_2, BN, CN, Si, and BO_2 negative ions over the first 120 nm from the postgrowth Fe catalyst surface of the SiO_2(500 nm) sample from Figure 3. The immediate surface region (<1 nm) contains a nitrogen rich composition with BN and CN species distributed across the surface, with the latter likely originating from air exposure. Although greatly decreased in concentration, both are still detected over the total sputtered depth. We note that the BN tends to be located at more specific points, possibly along Fe grain boundaries and edges. Once this nitrogen containing surface layer is removed, the next ∼6 nm are dominated by oxygen containing species of Fe, B, and Si (shaded gray area in Figure 4b). Subsequently, we see an increase in the Fe_2^- ion signal indicating sputtering of oxide free molecular Fe from the deposited layer. With increased depth from the surface, we begin to see an increase in the BO_2^- signal indicating an increased oxide concentration closer to the Fe/SiO_2 interface. The Si^- signal is detectable at the surface and shows a very small and gradual increase with depth. There is no evidence of an N^- ion signal at any location over the sputtered region as nitrogen does not readily form a negative ion, but a small atomic B^- related ion signal is detected confined to the near surface region (which is possibly due to areas of unreacted B, or decomposition of BO during sputtering). Combined, the SIMS observations support the in situ XRD data showing B and N uptake into the Fe catalyst in particular near the film surface, as well as again confirming the presence of Si throughout the films. We note that all SIMS signals here are influenced by air exposure during storage as discussed in further detail in the Supporting Information (see Figure S10).

Discussion. We first outline the general growth scenario for graphene CVD on catalyst surfaces, which represents a somewhat simpler monoelemental model system for understanding 2D material growth. It is worth pointing out that the understanding of graphene CVD remains incomplete, but numerous detailed growth studies for different catalysts and conditions across the literature allow some first-order growth model generalizations[8,10,42,43] that will serve as a reference for our further discussion below. For an initially bare catalyst surface, the supply of carbon from precursor dissociation begins to fill the catalyst with carbon close to the surface, which is mediated by carbon diffusion into and out from the catalyst bulk.[5,11] On reaching the carbon solubility limit, the further supply of carbon causes a supersaturation leading to the nucleation and subsequent growth of graphene at the catalyst surface.[44] Following basic 2D nucleation models, graphene nucleation is assumed to typically require a much higher supersaturation of C species compared to the subsequent growth phase,[42,43] and for each of these phases the rate limiting step for graphene growth can be different and may depend on growth conditions. Among the most important CVD parameters is temperature, which dictates several factors including the dissociation kinetics of the CVD precursor and the desorption and diffusivity of resulting species on and within the catalyst. The diffusion length or capture radius of growth species can thereby provide a minimum estimate of the graphene nucleation density. Catalyst surface imperfections, such as step edges, defects, and impurities, can be active sites for graphene nucleation.[8,10,42,45] Hence a passivation of such active sites by catalyst alloying or admixtures presents a pathway to lowering the graphene nucleation density, i.e., to achieve much larger graphene domain sizes.[8,10] It should be emphasized that the active catalyst surface is highly dynamic at the elevated temperatures and gas exposures typically used; hence as a basis for any growth model, it is of key importance to capture and understand the phase of the catalyst during CVD and its dynamic interactions with the precursors and growing 2D structure.

Figure 5a schematically illustrates the salient stages of the given h-BN CVD process and sets the context for our discussion on the crucial aspects of h-BN growth, as outlined in Figure 5b, including ternary and quaternary phase diagram considerations (Figure 5c). Prior to borazine introduction at ∼940 °C, the catalyst phase is almost entirely γ-Fe (fcc Fe, austenite) as expected given the phase transition from α-Fe (bcc Fe, ferrite) that occurs at ∼912 °C for elemental Fe.[39,40] During the annealing stage Si diffuses into the Fe, evidenced by ex situ SIMS and the formation of interfacial silicates observed by in situ XRD (Figure 5b, Step 1). The latter implies the partial breakdown of the interlayer by the formation of a fayalite phase at the expense of SiO_2,[46] and we thus propose that Si diffusion occurs due to the thermal instability of the Fe/SiO_2 and SiO_2/Si interfaces at 940 °C in oxygen deficient environments.[47,48] The Si concentration increases for thinner SiO_2 layers, and for SiO_2(200 nm) layers the appearance of "crater"-like features, rich in Si and to a lesser extent Fe (as confirmed by EDX, Figure S3c,d,e), indicates the onset of Fe silicidation, which is deleterious to h-BN growth. The dissociation of borazine during exposure supplies B and N species to the Fe surface (Figure 5b, Step 2), and based on the ternary Fe−B−N phase diagram (Figure 5c), the incorporation of B and N into the Fe catalyst as a solid solution is expected (Figure 5b, Step 3).[49] This is supported by our in situ XRD measurements, which evidence B uptake (via Fe-boride formation for extended borazine exposure, Figure 4a) and N uptake (via lattice expansion during NH_3 exposure control experiments, Figure S8) into the Fe catalyst surface region. Also our ex situ SIMS characterization further corroborates B and N uptake as shown by the presence of B and N containing species in the postgrowth Fe. During borazine exposure the Fe surface will continue to fill with B and N until the solubility limit is reached, corresponding to the incubation period prior to isothermal h-BN formation. Importantly for this ternary system (phase diagram sketch in Figure 5c), the interaction of the different solutes leads to a solubility limit and a subsequent phase evolution that depends on the relative proportions of B and N.[35−37] At the extremes of the solubility line, the nucleation of either just Fe-borides (B-rich end) or just Fe-nitrides (N-rich end) is expected; however, we exclude these growth trajectories for our conditions given that B and N are concurrently supplied by the borazine dissociation and that h-BN formation is confirmed following the growth process (even for exposure times where no Fe-boride formation is observed in XRD). Additionally, XPS measurements also reveal a B/N ratio of 1:1.03 ± 0.03 for the sample with SiO_2(200 nm) close to the surface (information depth ∼6 nm). Instead, on crossing the solubility line at an intermediate B−N ratio, a supersaturation of B and N develops at the surface leading to the nucleation of h-BN, which grows with continuing exposure (Figure 5b, Step 4) (this growth trajectory is indicated by the red arrow in Figure 5c). While some loss of dissociated N from the catalyst surface to the gas phase in the form of N_2 may additionally occur (Figure 5b, Step 5), we note that an intermediate B:N ratio appears to be maintained in the Fe catalyst, in contrast to Cu, for example, where the much larger solubility of B compared to N leads to growth occurring with predominantly

DOI: 10.1021/nl5046632
Nano Lett. 2015, 15, 1867−1875

B and negligible N diffusion into the catalyst bulk,[12] and also contrasting with previous suggestions regarding the mechanisms of boron nitride nanotube growth mechanisms from Fe catalysts.[35−37] No additional h-BN layer formation was observed ex situ for the optimized growth conditions, suggesting that growth occurs predominantly isothermally rather than by precipitation upon cooling.[8,44]

Our data shows that the h-BN nucleation density varies with the amount of Si in and on the Fe catalyst. It is well-known from heterogeneous catalysis that the chemical and structural state of the catalyst surface impacts its reactivity and selectivity.[45] As outlined above, prior literature on graphene CVD showed catalyst admixtures that lead to a lowering of the graphene nucleation density,[8] rationalized by the passivation of active catalyst sites. As highlighted by Figure 3, the situation here is clearly more complex: while going from Figure 3j to g, the initial increase in Si concentration leads to preferential nucleation of monolayer h-BN and a reduction in the number of h-BN nuclei, whereas a further increase in Si concentration from Figure 3g to d leads to a 5-fold increase in the h-BN nucleation density. When considering the role of Si the full complexity of the h-BN growth process (Figure 5) has to be taken into account. It is important to emphasize that relevant for h-BN nucleation and growth is the state and dynamics of the catalyst surface *during* the CVD process at elevated temperatures and gas exposure.

Given the low Si concentrations (<0.1 at. %, determined from XPS) present in samples with SiO_2 interlayers of 200 nm or more, the catalyst phase is γ-Fe prior to exposure as expected from literature[50] and the phase diagram of Figure 5c. The general catalyst phase evolution of Figure 5a remains relevant, at least for short growth times.[51] In the context of the basic framework outlined in Figure 5b, the Si admixture can in particular affect the catalytic dissociation of borazine (step 2) and the nucleation of h-BN (step 4). The growth behavior observed in Figures 3d,g,j can be rationalized by assuming that the Si locally reduces the supersaturation required to nucleate h-BN, meaning the onset of nucleation is reached more quickly and the precursor supply feeds fewer nuclei, which can thus grow to larger dimensions for the same exposure time (Figure 3j−g). Further Si addition (Figure 3g−d) then leads to a higher nucleation density. It is interesting to note that postgrowth analysis shows no obvious preference for h-BN nucleation to occur at Fe grain boundaries or craters (see Supporting Information, Figure S11). The series of Figures 3d,g,j also indicates a trend of increasing h-BN coverage with increasing Si concentration. This suggests that the Si admixture enhances the catalytic borazine dissociation. Similar to graphene CVD, the overall rate-limiting step for h-BN growth is bound to depend on the CVD conditions, and different kinetic processes can govern the different growth phases. The growth mode of h-BN domains on the catalyst surface can be limited by the incorporation kinetics of the constituent species (i.e. B and N) at the growth fronts or by the diffusion of the constituent species. For graphene CVD, the latter results in dendritic domain growth due to instabilities arising from growth front protrusions, whereas for the former the domain evolution can be described via kinematic Wulff constructions.[52] Due to the inequivalent sublattices, such Wulff constructions for h-BN or other compound 2D materials, including transition metal dichalcogenides,[53−55] result in much stricter geometric shapes, in agreement with the mostly triangular shaped h-BN domains observed here (Figures 1 and 3). Recent calculations[52] indicate

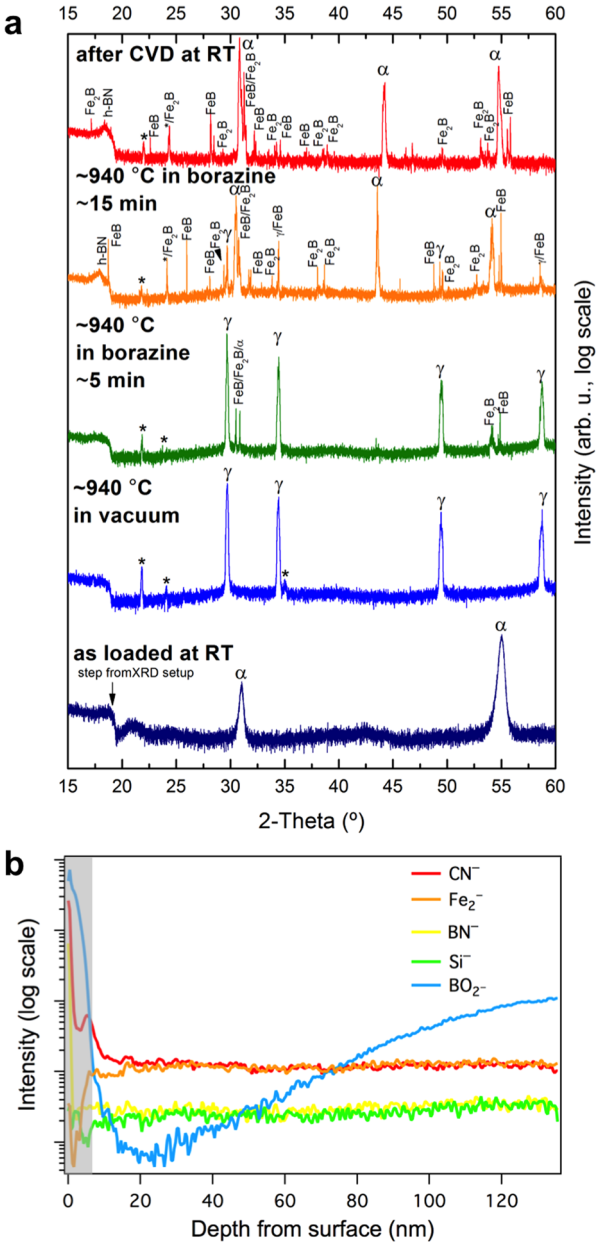

Figure 4. (a) Surface sensitive in situ XRD patterns of a Fe/SiO_2(300 nm)/Si sample during the salient stages of the CVD process. Fe undergoes a thermally induced phase transformation from as-deposited α-Fe to γ-Fe upon heating to 940 °C. Vacuum annealing at 940 °C leads to the appearance of reflections that can be ascribed to iron silicates, Fe_2SiO_4 (labeled with "*"). Upon borazine exposure (1×10^{-3} mbar) isothermal h-BN growth is indicated by the appearance of a reflection at ~18°. For short (5 min) borazine exposure the catalyst phase stays predominantly γ-Fe, while for extended (15 min) borazine feeding the appearance of Fe-boride phases (FeB and Fe_2B) indicates B dissolution into Fe, and an isothermal transformation of γ-Fe to α-Fe is observed (possibly linked to further B and/or Si diffusion,[41] see Figure S9). The room temperature phase after CVD is almost fully α-Fe. We note that intensity is plotted here on a log scale to emphasize minority phases. Figure S7 shows the same data plotted on a linear scale. (b) SIMS depth distribution of the top 120 nm from the surface of B, N, Si, and Fe related species of a Fe/SiO_2(500 nm)/Si sample, indicating a number of distinct regions of material distribution, showing a nitrogen rich surface layer followed by an oxygen rich region over the next ~6 nm (shaded area). The h-BN was grown for 5 min at 940 °C and 3×10^{-3} mbar.

DOI: 10.1021/nl5046632
Nano Lett. 2015, 15, 1867−1875

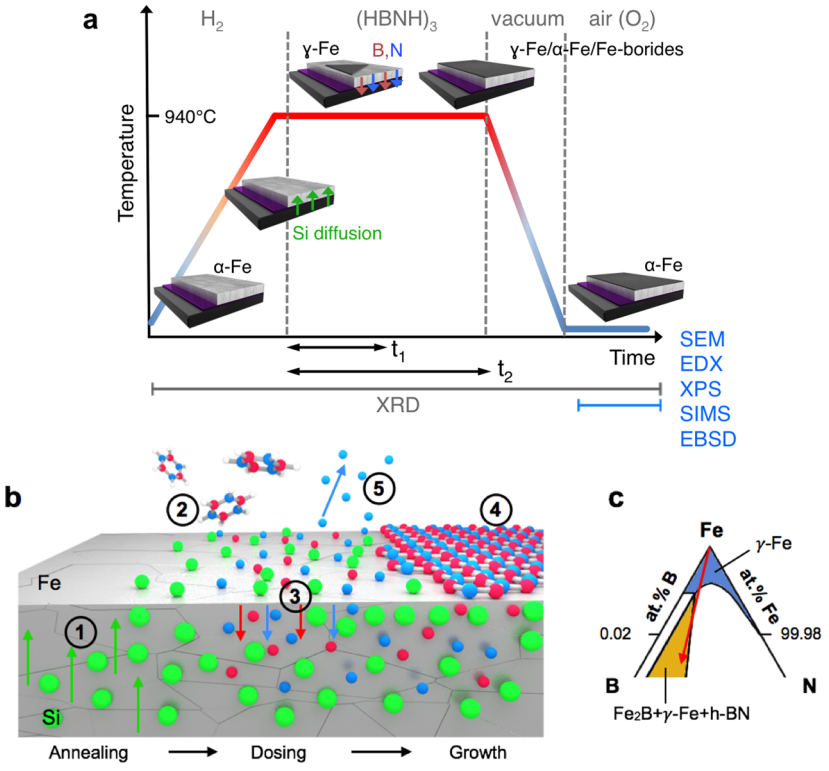

Figure 5. (a) Schematic illustrating the salient stages of the CVD process for the conditions used in this work. The 3D diagrams depict the state of the catalyst system during these steps, and the green, red, and blue arrows indicate the incorporation of Si, B and N into the Fe bulk, respectively. We note that the Fe undergoes a phase transformation during annealing, which reverts either upon cooling after short borazine exposure times (t_1) or isothermally at temperature for longer borazine exposure times (t_2). The gray labels on the bottom of the schematic indicate at which stages the various characterization techniques were performed. (b) Schematic of the growth model for h-BN CVD on Fe/SiO_2/Si substrates: (1) Annealing: onset of Si diffusion into the catalyst; (2) exposure: the borazine molecules impinge on the surface where they dehydrogenate and dissociate; (3) B and N species diffuse into the Fe catalyst; (4) nucleation and growth of h-BN; (5) possible desorption of surface N to gas phase. (c) detail of the Fe-rich corner of the Fe−B−N ternary phase diagram in the isothermal section at 950 °C.[49] The blue region corresponds to the solid solution of B and N in γ-Fe. The yellow region corresponds the three-phase equilibrium of Fe_2B, γ-Fe, and h-BN. The red arrow indicates the suggested reaction pathway during CVD of h-BN on Fe films.

that diffusion instabilities in this case lead to sawtoothed edge geometries, exactly as we observe here for our lower pressure borazine exposures (Figures 1b and 3). The exploration of the richness of these interactions for 2D compound materials is beyond the scope of this paper, but the discussion highlights the importance of our data here in establishing a first-order framework to guide further progress and to foster a more detailed understanding of the specific growth mechanisms.

Conclusions. In summary we have shown that catalyst engineering allows a significant level of improvement and control of nucleation and growth of h-BN layers. We focus on a simple thin-film catalyst model system, based on physical vapor deposited Fe on oxidized Si wafer support. Our systematic characterization shows that by tuning the SiO_2 thickness the amount of Si supplied to the Fe catalyst can be carefully controlled. This Si admixture, albeit just at trace levels, allows us to exclusively nucleate monolayer h-BN and to demonstrate h-BN single crystal domains with lateral dimensions of ∼0.3 mm as well as continuous h-BN monolayer films with large domain sizes (>25 μm). Our data gives insights into the complex growth mechanisms, with both B and N dissolving into the Si-doped Fe catalyst. We rationalize the role of Si in terms of the underlying framework of heterogeneous catalysis. We believe that the insights gained establish a basis for further rational catalyst design for controlled compound 2D material CVD. We note that there are many possible routes to deliver the nucleation promoter, here Si, including for instance addition via the CVD gas atmosphere or prealloying in catalyst foils. Our results here can not only be generalized in terms of processing routes, but we expect that the findings are also highly relevant to the CVD of other compound 2D materials in particular to enhance their scalable growth control, as required for most future applications.

Methods. *h-BN Growth.* The substrates are prepared by sputter deposition of 1 μm of Fe (Lesker target 99.99% purity) on $SiO_2(x)$/Si wafers (PI-KEM, where x is native (∼1 nm), 200, 300, 500, and 2000 nm), sapphire (Alfa Aesar, EPI one-side polished, C-axis) and quartz (Spectrosil B Polished Windows). We note that Si wafers have very low B contents <26 ppb, thus not impacting our characterization. The h-BN films are grown in a customized Aixtron BM3 cold-wall reactor (base pressure 1×10^{-6} mbar). In this work we define the standard CVD parameters for growth of h-BN as 5 min borazine $(HBNH)_3$ exposure at a temperature of 940 °C and at a total pressure of 1×10^{-3} mbar. The samples are typically heated in 3.6 mbar of H_2 at 250 °C/min up to 750 °C and then at 50 °C/min up to 940 °C. After 2 min annealing at 940 °C the H_2 is removed. Borazine is dosed into the chamber through a leak valve (from a liquid reservoir), and after 5 min growth time the borazine leak valve is closed and the heater is turned off. Samples are cooled in vacuum.

DOI: 10.1021/nl5046632
Nano Lett. 2015, 15, 1867−1875

Transfer. For Raman spectroscopy, optical microscopy, and atomic force microscopy, we transfer the h-BN via the electrochemical bubbling method.[56] We perform the transfer by spin coating a support layer of poly(methyl methacrylate) (PMMA) at 5000 rpm for 40 s onto the h-BN. The sample is placed in a NaOH bath (1 M) that serves as electrolyte, and two platinum wires are used as electrodes. The Pt anode is immersed in the solution, whereas the Pt cathode is contacted with the sample. During electrolysis H_2 bubbles evolve at the h-BN/Fe interface, lifting the film from the substrate. The PMMA/h-BN film is rinsed in deionized (DI) water and scooped onto a SiO_2(300 nm)/Si wafer where it is left to dry. The PMMA is removed by immersing the sample in acetone for ∼12 h, followed by a rinse in IPA.

Characterization. For the ex situ characterization of the h-BN on the catalyst, we use scanning electron microscopy (SEM, Zeiss SigmaVP, 2 kV). For compositional analysis, we employ energy dispersive X-ray spectroscopy (EDX, 20 kV). Optical images are acquired using a Nikon eclipse ME600L microscope. AFM imaging is performed using a Nanoscope 3000 instrument, and the data for the height profile are analyzed using Gwyddion (images have been leveled using a path leveling tool). Raman spectroscopy is performed with a Renishaw Raman InVia microscope, using a 50× objective lens and a 532 nm laser excitation. TEM analysis is conducted using a Tecnai F20 microscope operated at 200 kV, with the h-BN film placed on a holey carbon film/copper mesh TEM grid (Agar Scientific, 200 copper mesh S147H). Ex situ XPS for the determination of the levels of Si, B, and N present was carried out using a monochromated Al Kα source (E_{photon} = 1486.7 eV) using a Kratos AXIS Ultra DLD XPS instrument at the National Physical Laboratory (UK). CasaXPS software was used to measure the peak areas using a linear or Tougaard background as appropriate, with the NPL transmission function (intensity) calibration and average matrix relative sensitivity factors (AMRSF), to determine the concentrations of the detectable elements present.[57] The energy scale is regularly calibrated to ISO 15472, and the position of the carbon 1s peak at 284.5 eV was checked to ensure peaks were at the correct binding energy positions. In situ X-ray diffraction (XRD) measurements are conducted at the European Synchrotron Research Facility (beamline BM20/ROBL) in a previously described setup[8,58] using a X-ray wavelength of 1.078 Å. Surface-sensitive measurements are acquired in grazing incidence geometry (angle of incidence 0.5°, information depth estimated to ∼100 nm) while bulk-sensitive measurements (information depth in the μm range) are acquired in symmetric θ–2θ geometry (sample tilted out of plane by 3° to suppress reflections from the single crystalline wafer substrates). We note that the step at ∼19° is due to the arrangement of detector and X-ray entrance/exit slits into the reaction chamber and that reflection positions shift between room temperature and CVD temperature scans due to thermal expansion. Phase identification is undertaken by comparison to the Inorganic Crystal Structure Database (ICSD) (α-Fe: 53451, γ-Fe: 44862, Fayalite Fe_2SiO_4: 4353, Fe_2B: 391330, FeB: 391331, ε-Fe_xN: 80930, γ'-Fe_4N: 79980, h-BN: 167799) and International Center for Diffraction Data (ICDD) database (Fe_2SiO_4: 711670, Fe_2B: 361332, FeB: 320463). Secondary ion mass spectrometry (SIMS) measurements are performed at the National Physical Laboratory (UK) using a TOF-SIMS IV time-of-flight secondary ion mass spectrometer (ION-TOF GmbH, Germany), equipped with a dual source column for sputtering and a liquid metal ion gun at an angle of 45° to the surface normal. The depth calibration is based on a calculation of the sputter rate of Fe using Cs^+ ions at 10 keV and an ion current of 20 nA over a sputter area of 400 × 400 μm, giving a sputter rate of ∼0.064 (±3%) nm/s. The analysis beam consists of Bi^{3+} ions operated at 25 keV, with an ion current of 0.1 pA, randomly rastered over an area of 150 μm × 150 μm in the center of the sputter crater. To compare the relative concentration of Si in each of the samples in Figure S5, the ratio of the Si^- ion signal to the Fe_2^- ion signal is compared, as due to variations in the sample grain structures, which in turn have different ionization potentials for the same ions, as well as variations in the oxygen content distributed in the samples, means that a direct comparison of the silicon signals is not possible. The Fe_2^- signal from the deposited Fe layer is used to provide a constant comparison as this signal is unlikely to be affected by contributions from sputter generated species. An electron flood gun generating 20 eV electrons is used to compensate for surface charging.

■ ASSOCIATED CONTENT

Supporting Information

Further h-BN growth data for different exposure pressures, alternative substrates, and specific sample regions. Electron backscatter diffraction (EBSD) characterization and further details of XRD and SIMS analysis. This material is available free of charge via the Internet at http://pubs.acs.org.

■ AUTHOR INFORMATION

Corresponding Author

*E-mail: sh315@cam.ac.uk.

Notes

The authors declare no competing financial interest.

■ ACKNOWLEDGMENTS

S.C. acknowledges funding from EPSRC (Doctoral training award). R.S.W. acknowledges a Research Fellowship from St. John's College. B.C.B acknowledges a Research Fellowship at Hughes Hall. A.C.-V. acknowledges the Conacyt Cambridge Scholarship and Roberto Rocca Fellowship. S.H. acknowledges funding from ERC grant InsituNANO (No. 279342). B.B., S.J.S., K.M., and A.J.P. would like to acknowledge the National Measurement Office (NMO) for funding through the Innovation, Research and Development (IRD) programme (Project No. 115948). We acknowledge the European Synchrotron Radiation Facility (ESRF) for provision of synchrotron radiation, and we thank the staff for assistance in using beamline BM20/ROBL. We would also like to acknowledge Prof. Bonnie J. Tyler for discussions related to the manuscript.

■ REFERENCES

(1) Novoselov, K. S.; Fal'ko, V. I.; Colombo, L.; Gellert, P. R.; Schwab, M. G.; Kim, K. *Nature* **2012**, *490*, 192–200.

(2) Butler, S. Z.; Hollen, S. M.; Cao, L.; Cui, Y.; Gupta, J. A.; Gutie, H. R.; Heinz, T. F.; Hong, S. S.; Huang, J.; Ismach, A. F.; Johnston-Halperin, E.; Kuno, M.; Plashnitsa, V. V.; Robinson, R. D.; Ruoff, R. S.; Salahuddin, S.; Shan, J.; Shi, L.; Spencer, O. M. G.; Terrones, M.; Windl, W.; Goldberger, J. E. *ACS Nano* **2013**, *7*, 2898–2926.

(3) Fiori, G.; Bonaccorso, F.; Iannaccone, G.; Palacios, T.; Neumaier, D.; Seabaugh, A.; Banerjee, S. K.; Colombo, L. *Nat. Nanotechnol.* **2014**, *9*, 768–779.

(4) Focus Issue in *Nat. Nanotechnol.* **2014**, *9*, 725–807.

DOI: 10.1021/nl5046632
Nano Lett. 2015, 15, 1867–1875

(5) Weatherup, R. S.; Amara, H.; Blume, R.; Dlubak, B.; Bayer, B. C.; Diarra, M.; Bahri, M.; Cabrero-Vilatela, A.; Caneva, S.; Kidambi, P. R.; Martin, M.-B.; Deranlot, C.; Seneor, P.; Schloegl, R.; Ducastelle, F.; Bichara, C.; Hofmann, S. *J. Am. Chem. Soc.* **2014**, *136*, 13698−13708.
(6) Patera, L.; Africh, C.; Weatherup, R.; Blume, R.; Bhardwaj, S.; Castellarin-Cudia, C.; Knop-Gericke, A.; Schloegl, R.; Comelli, G.; Hofmann, S.; Cepek, C. *ACS Nano* **2013**, *7*, 7901−7912.
(7) Kidambi, P. R.; Bayer, B. C.; Blume, R.; Wang, Z.-J.; Baehtz, C.; Weatherup, R. S.; Willinger, M.-G.; Schloegl, R.; Hofmann, S. *Nano Lett.* **2013**, *13*, 4769−4778.
(8) Weatherup, R. S.; Bayer, B. C.; Blume, R.; Ducati, C.; Baehtz, C.; Schlögl, R.; Hofmann, S. *Nano Lett.* **2011**, *11*, 4154−4160.
(9) Li, X.; Magnuson, C. W.; Venugopal, A.; An, J.; Suk, J. W.; Han, B.; Borysiak, M.; Cai, W.; Velamakanni, A.; Zhu, Y.; Fu, L.; Vogel, E. M.; Voelkl, E.; Colombo, L.; Ruoff, R. S. *Nano Lett.* **2010**, *10*, 4328−4334.
(10) Hao, Y.; Bharathi, M. S.; Wang, L.; Liu, Y.; Chen, H.; Nie, S.; Wang, X.; Chou, H.; Tan, C.; Fallahazad, B.; Ramanarayan, H.; Magnuson, C. W.; Tutuc, E.; Yakobson, B. I.; McCarty, K. F.; Zhang, Y.-W.; Kim, P.; Hone, J.; Colombo, L.; Ruoff, R. S. *Science* **2013**, *342*, 720−723.
(11) Weatherup, R. S.; Dlubak, B.; Hofmann, S. *ACS Nano* **2012**, *6*, 9996−10003.
(12) Kidambi, P. R.; Blume, R.; Kling, J.; Wagner, J. B.; Baehtz, C.; Weatherup, R. S.; Schloegl, R.; Bayer, B. C.; Hofmann, S. *Chem. Mater.* **2014**, *26*, 6380−6392.
(13) Lin, Y.; Connell, J. W. *Nanoscale* **2012**, *4*, 6908−6939.
(14) Ci, L.; Song, L.; Jin, C.; Jariwala, D.; Wu, D.; Li, Y.; Srivastava, A.; Wang, Z. F.; Storr, K.; Balicas, L.; Liu, F.; Ajayan, P. M. *Nat. Mater.* **2010**, *9*, 430−435.
(15) Lee, K. H.; Shin, H.-J.; Lee, J.; Lee, I.; Kim, G.-H.; Choi, J.-Y.; Kim, S.-W. *Nano Lett.* **2012**, *12*, 714−718.
(16) Song, L.; Ci, L.; Lu, H.; Sorokin, P. B.; Jin, C.; Ni, J.; Kvashnin, A. G.; Kvashnin, D. G.; Lou, J.; Yakobson, B. I.; Ajayan, P. M. *Nano Lett.* **2010**, *10*, 3209−3215.
(17) Kim, K. K.; Hsu, A.; Jia, X.; Kim, S. M.; Shi, Y.; Hofmann, M.; Nezich, D.; Rodriguez-Nieva, J. F.; Dresselhaus, M.; Palacios, T.; Kong, J. *Nano Lett.* **2012**, *12*, 161−166.
(18) Kim, G.; Jang, A.-R.; Jeong, H. Y.; Lee, Z.; Kang, D. J.; Shin, H. S. *Nano Lett.* **2013**, *13*, 1834−1839.
(19) Gao, Y.; Ren, W.; Ma, T.; Liu, Z.; Zhang, Y.; Liu, W.-B.; Ma, L.-P.; Ma, X.; Cheng, H.-M. *ACS Nano* **2013**, *7*, 5199−5206.
(20) Park, J.-H.; Park, J. C.; Yun, S. J.; Kim, H.; Luong, D. H.; Kim, S. M.; Choi, S. H.; Yang, W.; Kong, J.; Kim, K. K.; Lee, Y. H. *ACS Nano* **2014**, *8*, 8520−8528.
(21) Chatterjee, S.; Luo, Z.; Acerce, M.; Yates, D. M.; Johnson, A. T. C.; Sneddon, L. G. *Chem. Mater.* **2011**, *23*, 4414−4416.
(22) Liu, Z.; Gong, Y.; Zhou, W.; Ma, L.; Yu, J.; Idrobo, J. C.; Jung, J.; MacDonald, A. H.; Vajtai, R.; Lou, J.; Ajayan, P. M. *Nat. Commun.* **2013**, *4*, 2541.
(23) Shi, Y.; Hamsen, C.; Jia, X.; Kim, K. K.; Reina, A.; Hofmann, M.; Hsu, A. L.; Zhang, K.; Li, H.; Juang, Z.-Y.; Dresselhaus, M. S.; Li, L.-J.; Kong, J. *Nano Lett.* **2010**, *10*, 4134−4139.
(24) Orofeo, C. M.; Suzuki, S.; Kageshima, H.; Hibino, H. *Nano Res.* **2013**, *6*, 335−347.
(25) Vinogradov, N. A.; Zakharov, A. A.; Ng, M. L.; Mikkelsen, A.; Lundgren, E.; Mårtensson, N.; Preobrajenski, A. B. *Langmuir* **2012**, *28*, 1775−1781.
(26) Morscher, M.; Corso, M.; Greber, T.; Osterwalder, J. *Surf. Sci.* **2006**, *600*, 3280−3284.
(27) Ćavar, E.; Westerström, R.; Mikkelsen, A.; Lundgren, E.; Vinogradov, A. S.; Ng, M. L.; Preobrajenski, A. B.; Zakharov, A. A.; Mårtensson, N. *Surf. Sci.* **2008**, *602*, 1722−1726.
(28) Müller, F.; Grandthyll, S. *Surf. Sci.* **2013**, *617*, 207−210.
(29) Simonov, K. A.; Vinogradov, N. A.; Ng, M. L.; Vinogradov, A. S.; Mårtensson, N.; Preobrajenski, A. B. *Surf. Sci.* **2012**, *606*, 564−570.
(30) Allan, M. P.; Berner, S.; Corso, M.; Greber, T.; Osterwalder, J. *Nanoscale Res. Lett.* **2007**, *2*, 94−99.
(31) Sutter, P.; Lahiri, J.; Albrecht, P.; Sutter, E. *ACS Nano* **2011**, *5*, 7303−7309.
(32) Corso, M.; Auwärter, W.; Muntwiler, M.; Tamai, A.; Greber, T.; Osterwalder, J. *Science* **2004**, *303*, 217−220.
(33) Takahashi, T.; Itoh, H.; Takeuchi, A. *J. Cryst. Growth* **1979**, *47*, 245−250.
(34) Tay, R. Y.; Griep, M. H.; Mallick, G.; Tsang, S. H.; Singh, R. S.; Tumlin, T.; Teo, E. H. T.; Karna, S. P. *Nano Lett.* **2014**, *14*, 839−846.
(35) Su, C.-Y.; Chu, W.-Y.; Juang, Z.-Y.; Chen, K.-F.; Cheng, B.-M.; Chen, F.-R.; Leou, K.-C.; Tsai, C.-H. *J. Phys. Chem. C* **2009**, *113*, 14732−14738.
(36) Koi, N.; Oku, T.; Nishijima, M. *Solid State Commun.* **2005**, *136*, 342−345.
(37) Arenal, R.; Stephan, O.; Cochon, J.; Loiseau, A. *J. Am. Chem. Soc.* **2007**, *129*, 16183−16189.
(38) Gorbachev, R. V.; Riaz, I.; Nair, R. R.; Jalil, R.; Britnell, L.; Belle, B. D.; Hill, E. W.; Novoselov, K. S.; Watanabe, K.; Taniguchi, T.; Geim, A. K.; Blake, P. *Small* **2011**, *7*, 465−468.
(39) Wriedt, H.; Gokcen, N.; Nafziger, R. *Bull. Alloy Phase Diagr.* **1987**, *8*, 355−377.
(40) Okamoto, H. *J. Phase Equilib. Diffus.* **2004**, *25*, 297−298.
(41) Raghavan, V. *J. Phase Equilib. Diffus.* **2007**, *28*, 380−381.
(42) Kim, H.; Mattevi, C.; Calvo, M. R.; Oberg, J. C.; Artiglia, L.; Agnoli, S.; Hirjibehedin, C. F.; Chhowalla, M.; Saiz, E. *ACS Nano* **2012**, *6*, 3614−3623.
(43) Loginova, E.; Bartelt, N. C.; Feibelman, P. J.; McCarty, K. F. *New J. Phys.* **2009**, *11*, 063046.
(44) Weatherup, R. S.; Bayer, B. C.; Blume, R.; Baehtz, C.; Kidambi, P. R.; Fouquet, M.; Wirth, C. T.; Schlögl, R.; Hofmann, S. *ChemPhysChem* **2012**, *13*, 2544−2549.
(45) Vang, R. T.; Honkala, K.; Dahl, S.; Vestergaard, E. K.; Schnadt, J.; Laegsgaard, E.; Clausen, B. S.; Nørskov, J. K.; Besenbacher, F. *Nat. Mater.* **2005**, *4*, 160−162.
(46) Bendersky, L. A.; Kazantseva, N. V.; Kattner, U. R.; Wang, K.; Oleshko, V. P.; Hunter, D.; Takeuchi, I. *Acta Mater.* **2013**, *61*, 4180−4190.
(47) Liehr, M. *J. Vac. Sci. Technol. A* **1987**, *5*, 1559−1562.
(48) Zhang, C.-H.; Wan, H.-J.; Yang, Y.; Xiang, H.-W.; Li, Y.-W. *Catal. Commun.* **2006**, *7*, 733−738.
(49) Schuster, J. C. *ASM Int.* **1992**, 32−37.
(50) Lacaze, J.; Sundman, B. *Metall. Trans. A* **1991**, *22*, 2211−2223.
(51) Fountain, R. W.; Chipman, J. *Trans. Met. Soc. AIME* **1962**, *224*, 599−606.
(52) Artyukhov, V. I.; Yakobson, B. I.; Hao, Y.; Ruo, R. S. Preprint at: *arXiv:1405.5799*.
(53) Liu, Y.; Bhowmick, S.; Yakobson, B. I. *Nano Lett.* **2011**, *11*, 3113−3116.
(54) Van der Zande, A. M.; Huang, P. Y.; Chenet, D. A.; Berkelbach, T. C.; You, Y.; Lee, G.-H.; Heinz, T. F.; Reichman, D. R.; Muller, D. A.; Hone, J. C. *Nat. Mater.* **2013**, *12*, 554−561.
(55) Zhang, Y.; Zhang, Y.; Ji, Q.; Ju, J.; Yuan, H.; Shi, J.; Gao, T. *ACS Nano* **2013**, *7*, 8963−8971.
(56) Gao, L.; Ren, W.; Xu, H.; Jin, L.; Wang, Z.; Ma, T.; Ma, L.-P.; Zhang, Z.; Fu, Q.; Peng, L.-M.; Bao, X.; Cheng, H.-M. *Nat. Commun.* **2012**, *3*, 699.
(57) Seah, M. P.; Gilmore, I. S.; Spencer, S. J. *J. Elect. Spect.* **2001**, *120*, 93−111.
(58) Bayer, B. C.; Baehtz, C.; Kidambi, P. R.; Weatherup, R. S.; Mangler, C.; Kotakoski, J.; Goddard, C. J. L.; Caneva, S.; Cabrero-Vilatela, A.; Meyer, J. C.; Hofmann, S. *Appl. Phys. Lett.* **2014**, *105*, 143111.
(59) Spizzirri, P. G.; Rubanov, S.; Gauja, E.; Prawer, S. *Mater. Forum* **2008**, *34*, 161−166.

DOI: 10.1021/nl5046632
Nano Lett. 2015, 15, 1867−1875